Supporting Information

N-doped Carbon Nanotubes enriched with graphitic Nitrogen in a Buckypaper configuration as efficient 3D electrodes for Oxygen Reduction to H_2O_2

Enrique Contreras[1,2], David Dominguez[2], Hugo Tiznado[2], Jonathan Guerrero-Sanchez[2], Noboru Takeuchi[2], Gabriel Alonso[2], Oscar E. Contreras[2], Mercedes T. Oropeza-Guzman[3] and Jose M. Romo-Herrera[2].

[1] Centro de Investigación Científica y de Educación Superior de Ensenada (CICESE), Posgrado en Ciencias en Nanociencias, Carretera Ensenada-Tijuana No. 3918, Zona Playitas, CP 22860, Ensenada, BC México.

[2] Centro de Nanociencias y Nanotecnología, Universidad Nacional Autónoma de México (CNyN-UNAM), Km 107 Carretera Tijuana-Ensenada, CP 22800 Ensenada, B.C., México.

[3] Centro de Graduados e Investigación en Química, Instituto Tecnológico de Tijuana, Blvd. Alberto Limón Padilla s/n, Mesa de Otay, CP 22500 Tijuana, B.C., México.

Figure S1 shows: a) C-C (sp2) peaks of the CNx samples at 284.6eV, b) to f) shows the XPS analysis for carbon samples where it can be observed the C-C (sp2) at 284.6eV, CO/COH at 286.3 eV, COO at 289 eV and a broad peak of π- π* at 291 eV **[1-2]**.

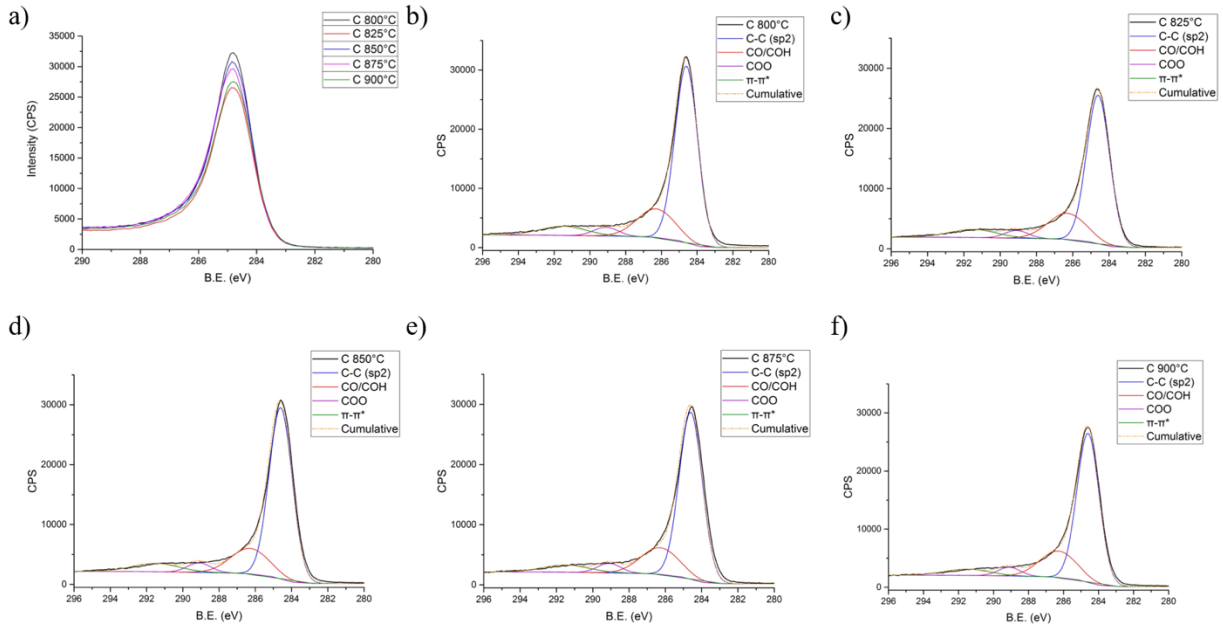

Figure S1. XPS C1s of the five samples of CNx.

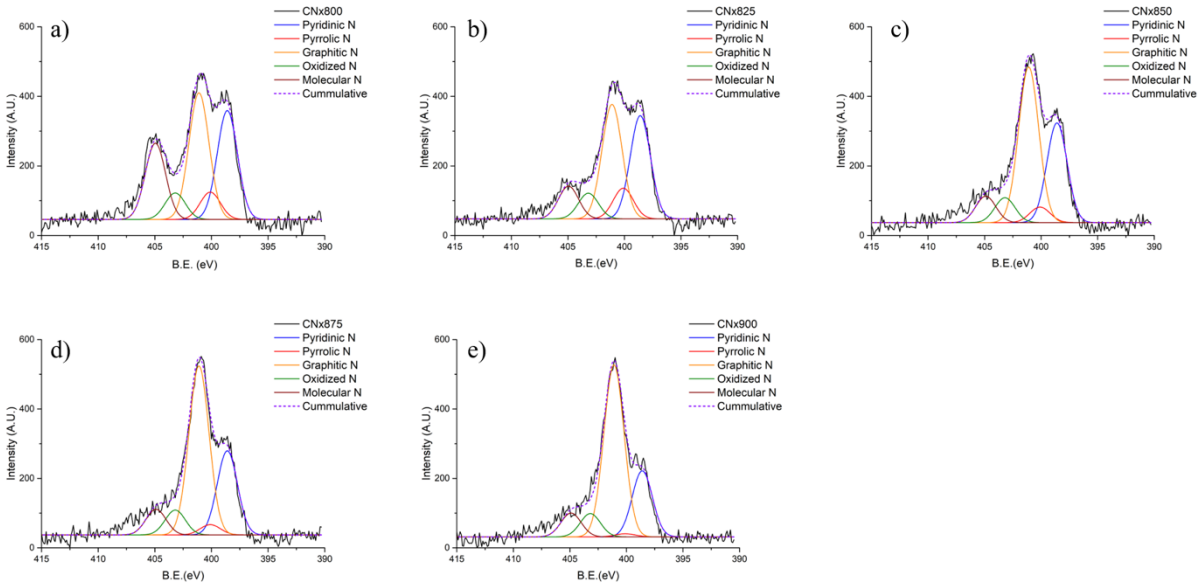

Figure S2. XPS N1s of the five samples of CNx.

Figure S2 shows the XPS analysis of N 1s where it can be observed the five different species of nitrogen in the carbon nanotubes; pyridinic nitrogen at 398.6 eV, pyrrolic nitrogen at 400.1 eV, graphitic nitrogen at 401.1 eV, oxidized nitrogen at 403.2 eV and molecular nitrogen at 404.9 eV **[1-7]**.

Figure S3a and S3b are representations of either hydrothermal process and vacuum filtering process to make the nitrogen-doped carbon nanotubes dispersions and the buckypapers. Figure S3c and S3d are real images of the hydrothermal process. For the hydrothermal process (HTP) we used 50 mg of carbon nanotubes in 1.7 L of DI water, as observed in figure S3e, CNTs can barely be seen. After the 5 hours of HTP, it is observed a colored black dispersion shown in figure S3f and S3g. Finally, after the HTP we proceed to vacuum filter the blackish solution obtaining the buckypaper shown in figure S3h.

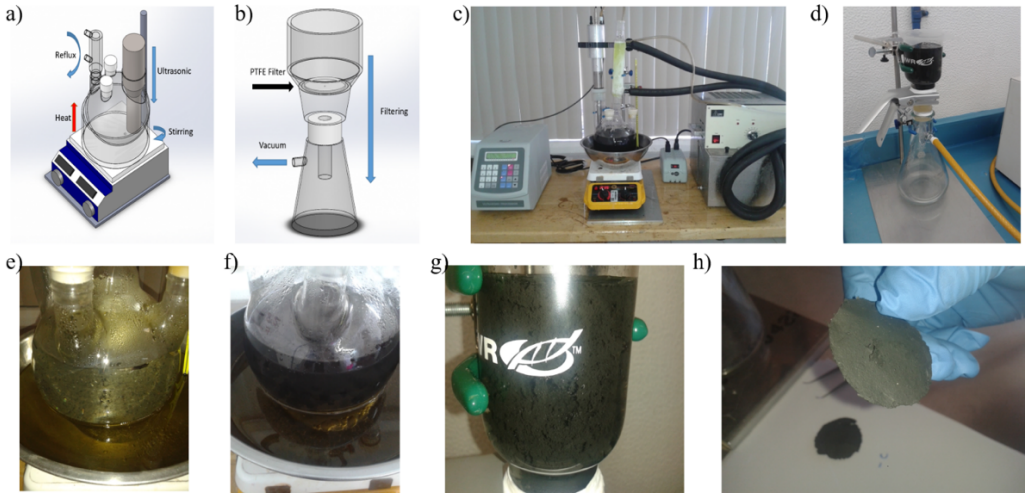

Figure S3. Hydrothermal process steps for the buckypaper fabrication.

The buckypapers obtained have a circular shape as it can be observed in figure S4a, after the buckypaper fabrication we trimmed the circumscribed square, and selected three different areas in the square: A1 with ~0.25cm^2; A2 with ~1cm^2 and A3 with ~2.25cm^2 (shown in figure S4b). The three different trimmed squares can be seen in figure S4c.

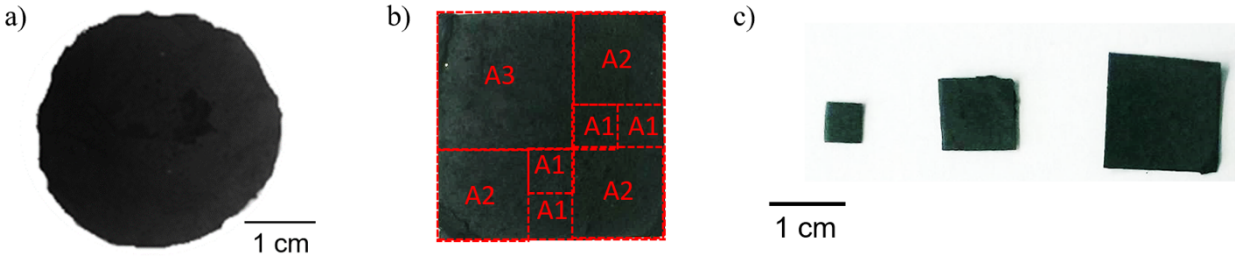

Figure S4. It is observed a) picture of a buckypaper, b) areas selected for trimming and c) the trimmed buckypaper squares.

The typical forest-like array obtained directly from the nanotubes synthesis is shown in the SEM picture in figure S5a and a higher magnification SEM image shows the densely packed aligned nanotubes in such arrays as shown in figure S5b. A representative TEM image is presented in figure S5c showing the typical bamboo-shape of the nitrogen-doped carbon nanotubes.

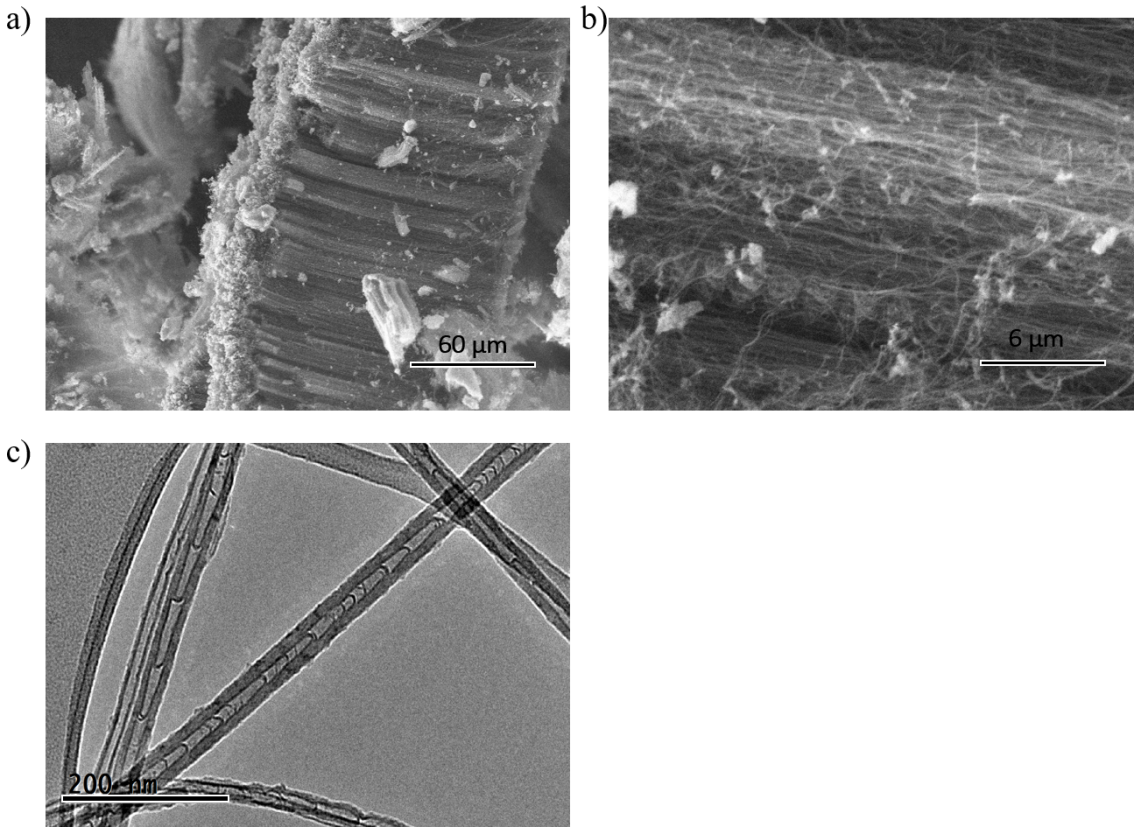

Figure S5. a) and b) are SEM images where it can be observed the forest-like arrays at 500X and 5000X respectively and c) is a TEM micrograph where it can be observed the bamboo structure typical of the CNx.

In order to complement the composition analysis of the nitrogen-doped carbon nanotubes we performed EDXS (Energy Dispersive X-rays Spectroscopy) mapping using Transmission Electron Microscopy in STEM (Scanning Transmission Electron Microscopy) mode. The electron image shows the HAADF (High Angle Annular Dark Field) image of the sample under analysis. The Carbon map shows not only the presence of the nanotubes but it includes the lacey carbon film from the TEM grid; similarly, the Oxygen presence is detected in the Oxygen map not only from the nanotubes location but more clearly from the lacey carbon film. However, when the Nitrogen signal is monitored in the Nitrogen map none signal is coming from the lacey carbon film, but only from the nanotubes locations, demonstrating the presence of Nitrogen at the carbon nanotubes.

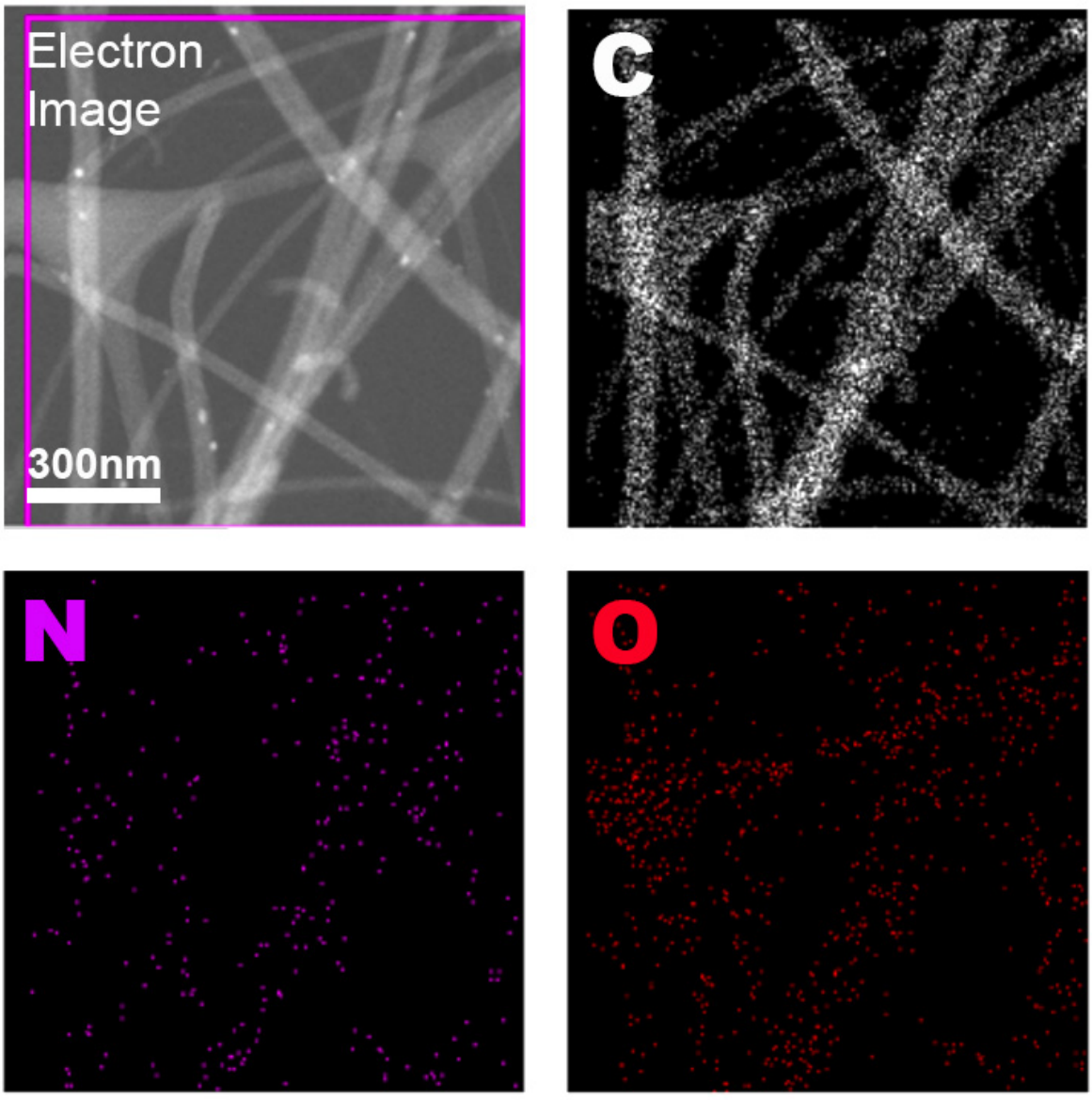

Figure S6. EDXS mapping from the CNx-900C sample taken in STEM mode using a TEM. HAADF image and Maps from Carbon, Oxygen and Nitrogen signal are presented.

Stability Test

Stability tests were performed using cyclic voltammetry at 100 mV/s for two samples: CNx800 and CNx900 for 1000 cycles.

The stability test showed a very good electrochemical stability of CNx900, while CNx800 displayed a slight improvement in its electrochemical activity. Both samples tend to the ~ 0.7 V vs RHE (the standard reduction potential for the ORR two-electron pathway).

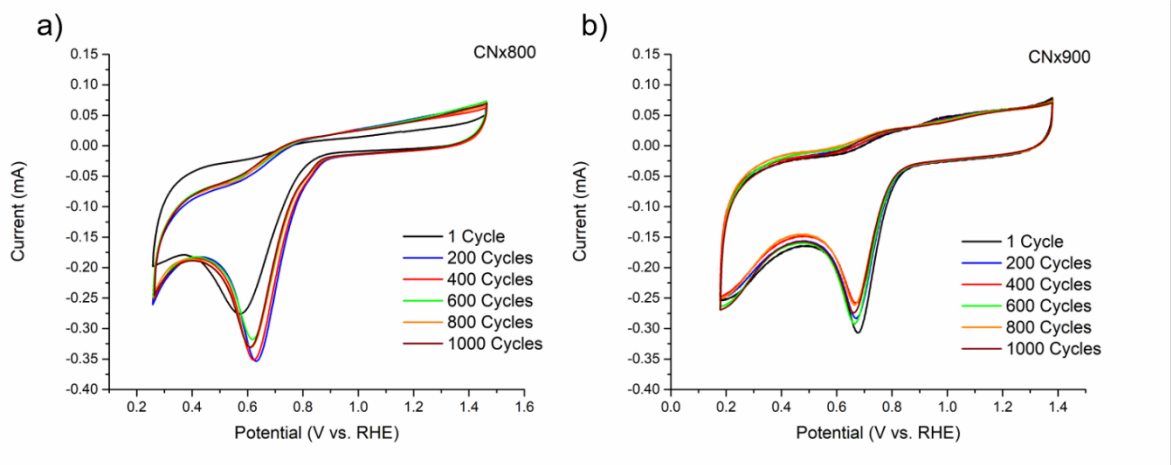

Figure S7. Stability tests performed from 1 to 1000 to: a) CNx 800 and b) CNx900

Figure S8 shows LSV normalized to the loading mass for alkaline media (Figure S3a and S3b) and neutral media (Figure S3c and S3d).

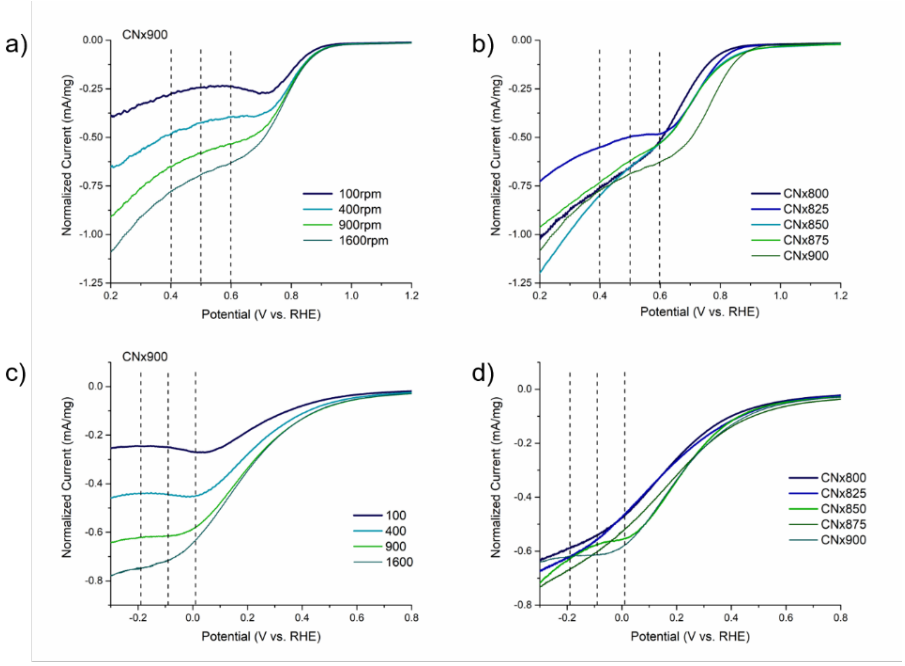

Figure S8. LSV normalized to load mass: a) is the CNx 900 at different rotation speeds at alkaline media, b) LSV of all samples at 1600 RPM in alkaline media, c) is the CNx 900 at different rotation speeds at neutral media and d) LSV of all samples at 1600 RPM in neutral media

Calculations for the electroactive surface area (EASA)

The EASA was obtained performing cyclic voltammetry using 5 mM $K_3Fe(CN)_6$ / 0.1 M KCl, at scan rate of 50 mV/s and calculated using the Randles-Sevcik equation:

$$i_p = 2.69x10^5 * n^{3/2} * A * D^{1/2} * V^{1/2} * C \quad (1)$$

Where, i_p is the current peak (A), n=1, D=4.34x10^{-6} (cm^2/s), V is the scan rate (V/s), C is the concentration (mol/mL). Solving for A and dividing by the mass loading we obtained the electroactive surface area (cm^2). **[8]**

The CV was performed preparing the electrode by depositing 0.2 mg of CNx on the surface of glassy carbon electrodes with a geometric area of 0.07 cm^2.

Table S1. Electroactive Surface Area of the different samples of nitrogen-doped carbon nanotubes.

Electrode	CNx800	CNx825	CNx850	CNx875	CNx900
EASA (cm^2/mg)	6.55	6.59	6.45	6.21	6.19

Estimation of the graphitic nitrogen sites per cm^2.

The population of graphitic Nitrogen sites present in our samples were estimated following equation 2:

$$Graphitic\ Nitrogen\ sites = W\left(\frac{mg}{cm^2}\right) * EASA\left(\frac{cm^2}{mg}\right) * D_{Atoms}\left(\frac{atoms}{cm^2}\right) * \rho_{graphiticN}(at\%) \quad (2)$$

where W is the catalyst loading deposited on the electrode, EASA was obtained by Randles-Sevcick equation (see previous section in the Supporting Information), D is the atomic carbon density in each graphite layer (3.82x10^{15} atoms/cm^2) and $\rho_{graphiticN}$ is the graphitic nitrogen in the different samples obtained by XPS.

Table S2. Estimation of the graphitic nitrogen sites per cm^2.

Sample	Catalyst loading (mg/cm^2)	EASA (cm^2/mg)	$\rho_{graphiticN}$ (at%)	Graphitic Nitrogen sites per cm^2 (N_{graph}/cm^2)
CNx800	2.86	6.55	0.75	5.36E+16
CNx825	2.86	6.59	0.76	5.44E+16
CNx850	2.86	6.45	0.94	6.62E+16
CNx875	2.86	6.21	1.01	6.86E+16
CNx900	2.86	6.19	1.07	7.22E+16

Proposed mechanism for graphitic Nitrogen favoring the ORR two-electron pathway.

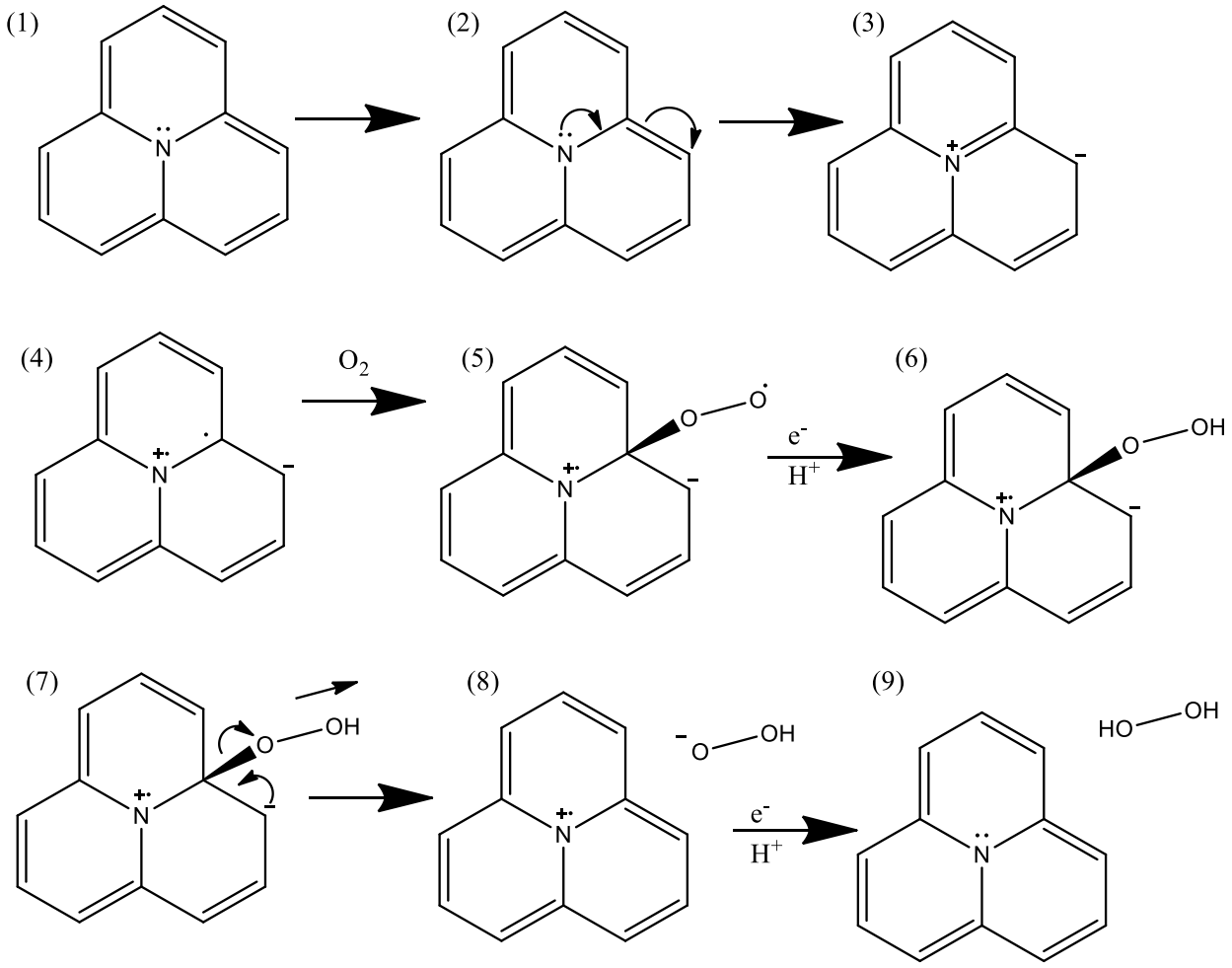

Figure S9. Proposed mechanism for the two-electron pathway ORR performed by graphitic nitrogen

The figure S9 presents the proposed mechanism for the two-electron pathway ORR by the graphitic nitrogen, it is worthy to note that all the carbons in the schemes are bonded to three carbon neighbors, and all the carbons are sp2 hybridized. The proposed mechanism can only occur under the polarization conditions.

The graphitic nitrogen has a pair of electrons in its p_z orbital, the electron pair makes a π bonding to an alpha carbon (carbon corresponding to the first neighbor), which turns the graphitic nitrogen to be positively charged and the beta carbon (carbon corresponding to the second nearest neighbor) is negatively charged (steps observed in figure S9 1-3).

An oxygen molecule can be bonded to the radical alpha carbon by free radical addition between the lone electron in the p_z and the lone electron in the π^* of the oxygen molecule; it is important to mention that the bond between the oxygen and alpha carbon has been previously

demonstrated by Guo *et al.* **[1]** while Sidik *et al.* showed that radical alpha carbon can play a role in the ORR **[9]**. The free radical addition it is observed in figure S9 4-5.

In order to start the ORR, one electron is supplied by the electrical polarization and one proton from the media, the hydrogen then can be bonded to the oxygen molecule by free radical addition, forming an hydroperoxide group bonded to the alpha carbon (as observed in figure S9 6).

However, the formed structure is quite unstable due to the unbalance of charges, then the negative charged beta carbon will tend to make a double bond with the alpha carbon releasing a negative charged hydroperoxide molecule (figure S9 7-8). The mechanism ends when a proton bonds a negative charged hydroperoxide and a second lone electron (supplied by the electrical polarization) recombines to the lone electron in the p_z orbital of the graphitic nitrogen (figure S9 9).

This mechanism outstands, that contrary to the pyridinic nitrogen, the graphitic N is unable to complete the four-electron reduction reaction to end up with a couple of water molecules due to the unbalance of charges (due to the negative charged beta carbon and positive charged graphitic nitrogen), making the graphitic N site to release the anchored molecule (hydroperoxide) which will end up as a H_2O_2 molecule, therefore completing the two-electron pathway favoring the H_2O_2 generation. When samples are enriched with pyridinic nitrogen, the oxygen reduction reaction could continue from the 2-electron pathway to the 2+2 electron pathway, since none unbalance for charges will push for the anchored molecule release.

References.

1 D. Guo, R. Shibuya, C. Akiba, S. Saji, T. Kondo and J. Nakamura, *Science*, 2016, **351**, 361-365.
2 S. Maldonado, S. Morin and K.J. Stevenson, *Carbon*, 2006, **44**, 1429-1437.
3 E. Raymundo-Pinero, D. Cazorla-Amoros, A. Linares-Solano, J. Find, U. Wild and R. Schlogl., *Carbon*, 2002, **40**, 597-608.
4 L.G. Bulusheva, A.V. Okotrub, I.A. Kinloch, I.P. Asanov, A.G. Kurenya, A.G. Kudashov, X. Chen and H. Song, *Phys. Status Solidi B*, 2008, **245**, 1971-1974.
5 J.R. Pels, F. Kapteijn, J.A. Moulijn, Q. Zhu and K.M. Thomas, *Carbon*, 1995, **33**, 1641-1653.
6 I. Kuzunoki, M. Sakai, Y. Igari, S. Ishidzuka, T. Takami, T. Takaoka, M. Nishitani-Gamo and T. Ando, *Surf. Sci.*, 2001, **492**, 315-328.
7 I. Zeferino Gonzalez, A.M. Valenzuela-Muniz, G. Alonso-Nunez, M.H. Farias and Y. Verde Gomez, *ECS J. Solid State Sci. and Technol.*, 2017, **6**: M3135-M3139.
8 Xue, Y., Liu, J., Chen, H., Wang, R., Li, D., Qu, J., & Dai, L. *Angewandte Chemie International Edition*. 2012. **51**. 12124-12127.
9 Sidik, R. A., Anderson, A. B., Subramanian, N. P., Kumaraguru, S. P., & Popov, B. N. *The Journal of Physical Chemistry B*, 2006, **110(4)**, 1787-1793.